A Grid-forming Control Method For DFIG Based on the Grid-side Converter

Yong Sun, Baoju Li
State Grid Jilin Electric Power Co., Ltd.
Changchun, China
sunyong_hit{libaoju1986}@163.com

Jiajun Zhang
Electric Power Research Institute
State Grid Jilin Electric Power Co., Ltd.
Changchun, China
15004300630@163.com

Yuwei Cheng,Wenchuan Wu, Chenhui Lin, Guannan Wu
Department of Electrical Engineering
Tsinghua University
Beijing, China
cyw23@mails.tsinghua.edu.cn,wuwench{linchenhui}@tsinghua.edu.cn,wuguannan722@163.com

***Abstract*—The growing penetration of renewable energy sources weakens the support from the grid to DFIGs, leading to potential instability in grid-following (GFL) DFIG systems. Grid-forming (GFM) DFIGs have emerged as a promising solution to enhance system stability under weak grid conditions. GFM DFIGs are typically realized through the rotor-side converter (RSC), which improves synchronization stability but compromises the accuracy and bandwidth of power control. To overcome this limitation, this paper proposes a GFM strategy based on the grid-side converter (GSC). The proposed approach enhances the stability of DFIG systems in weak grids without degrading power control performance. A detailed analysis of the synchronization stability is conducted, and simulation results validate the effectiveness of the proposed method.**

***Index Terms*—DFIG, grid-side converter, grid-forming control**

NOMENCLATURE

$\boldsymbol{u}_s$,$\boldsymbol{i}_s$	Stator voltage and current vectors
$\boldsymbol{u}_{gc}$, $\boldsymbol{i}_{gc}$	GSC voltage and current vectors
p_s, q_s, p_{gc}, q_{gc}	active and reactive power of stator and GSC
v_{dc}, c_f	DC bus voltage and capacitance
ω_g, ω_s, ω_r	Nominal, synchronous rotor angular frequency
θ_s, θ_{gc}^*	Stator voltage angle and GSC voltage reference angle
$k_{p,PLL}$, $k_{i,PLL}$	Proportional and integral gain of PLL
k_p, k_i	Proportional and integral gain of power controller
α,η,λ,ρ	power error, voltage error, DC voltage error and line impedance adaptation parameters of fVOC
$\boldsymbol{Z}_g$,$\boldsymbol{Z}_f$,$\boldsymbol{Z}_{vi}$	Grid impedance, filter impedance and virtual
r_{vi}, x_{vi}	Virtual resistance and inductance of GSC
$*$	Superscript for reference valueimpedance

This work was supported by the Science and Technology Project of State Grid (4000-202429062A-1-1-ZN).

I. INTRODUCTION

Currently, DFIGs primarily adopt GFL control, where synchronization is achieved using Phase-locked Loops (PLL). Such synchronization is affected by the strength of the grid [1]. However, with the penetration of renewable resources increasing, the grid can no longer provide strong support for DFIGs, leading to a series of synchronization stability issues [2], [3].

There are primarily two approaches to address this issue. The first approach improves local grid strength through installing ancillary equipments near wind farms, e.g. , synchronous compensators or large-capacity GFM energy storage systems. This method involves significantly higher investment and maintenance costs. The other approach involves applying GFM control on the voltage/flux vectors of stator or rotor to achieve power-based synchronization. Chen *et al.* [4] compared several GFM control strategies for offshore wind farms connected to diode rectifier-based HVDC systems. Shah *et al.* [5]developed a GFM method based on stator flux and virtual synchronous machine (VSM). Yan *et al.* [6] shows that GFM DFIGs can effectively mitigate SSR issues. Wang *et al.* [7] applied VSM to the rotor voltage. Zhang *et al.* [8] applied droop control to the stator voltage and proposed an ADRC-based voltage loop to enchance robustness. Huang *et al.* [9] used VSM to provide inertia response and introduced an auxiliary damping component to relax the constraints on the damping coefficient. Additionally, there are a series of studies focused on enhancing the stability [10] and fault ride-through capability of GFM DFIGs [11].

As the capacity of the machine is much larger than the converter, the aforementioned controls are all implemented through the RSC, while the impact of the GSC is often neglected. However, RSC GFM DFIG may have some issues.

979-8-3315-8138-1

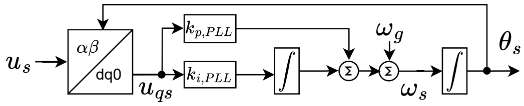

Fig. 1. Diagram of Phase-locked Loops.

Firstly, the inheret droop characteristics of GFM lead to inaccurate execution of power commands, necessitating additional compensation control to achieve functions such as MPPT. More critically, reliance on power synchronization results in a narrower power regulation bandwidth, causing traditional electromechanical damping control to fail and increasing the risk of electromechanical oscillations [12]. The electrical distance between the grid-side inverters and the induction motors is extremely short. Given this, converting the GSC to GFM voltage sources could be a potential approach. In this paper, some attempts are made in this regard:1) A RSC-based GFM DFIG control strategy is designed;2) Its small-signal stability is analysed; 3) Its effectiveness is verified by simulation experiments.

II. Design of Grid-forming DFIG based on GSC

A. Basic ideas

The diagram of PLL is given in Fig. 1. the PLL achieves synchronization of the stator by controlling the q-axis componet of PCC voltage u_{qs} to 0. Wang *et al.* derived the conditions for PLL synchronization stability [1]:

$$\|I_{pcc}\| < \frac{U_g}{|Z_T \sin(\theta_I + \phi_Z)|}, \tag{1}$$

where $\boldsymbol{i}_{pcc} = I_g \exp\{\mathrm{j}\theta_I\}$ is the current flow through the PCC in the reference frame of θ_s, U_g is the magnitude of grid voltage, $\boldsymbol{Z}_T = Z_T \exp\{\mathrm{j}\phi_Z\}$ is the equivalent impedance between the PCC and grid.

The idea of GFM GSC can be explained using Thevenin equivalent. The equivalent circuits are shown in the Fig. 2. In GFL DFIG (Fig. 2a), we have $\boldsymbol{Z}_{T,gfl} = \boldsymbol{Z}_g$ and $\boldsymbol{i}_{pcc,gfl} = \boldsymbol{i}_g$. As for GSC GFM DFIG (Fig. 2b), we have $\boldsymbol{i}_{pcc,gfl} = \boldsymbol{i}_s$. The Thevenin equivalent impedance can be calculated as $\boldsymbol{Z}_{T,gfm} = \boldsymbol{Z}_g(\boldsymbol{Z}_f + \boldsymbol{Z}_{vi})/(\boldsymbol{Z}_g + \boldsymbol{Z}_f + \boldsymbol{Z}_{vi})$ and the equivalent voltage approximates U_g. Assuming the power factor is identical in both cases, we have $U_g/|Z_{T,gfm}\sin(\theta_I + \phi_{Z,gfm})| > U_g/|Z_{T,gfl}\sin(\theta_I + \phi_{Z,gfl})|$ As a result, we can deduce that GSC GFM DFIG has better stability and stronger power transmission capability.

B. Control Implementation

The diagrm of GFM DFIG based on GSC is shown in Fig. 3. The mechanical part of the DFIG controls the rotor speed ω_r and provides the maximum power point P_{opt}. The slip ratio is $s = (\omega_s - \omega_r)/\omega_s$. The RSC operates in constant power mode using stator voltage vector orientated control [13]. Its active power reference P_s^* is given by $\min\{P_{opt}, P_{dis}\}$, where P_{dis} is the external dispatch command. This paper uses the full-state vitual oscillator (fVOC) as the GFM loop, which has

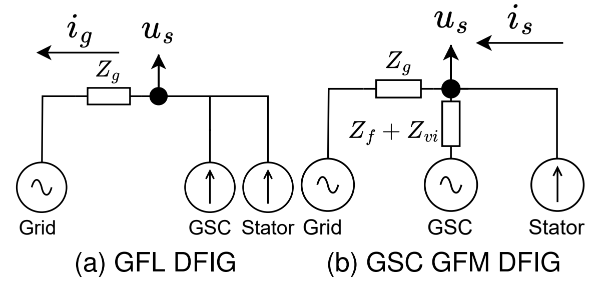

Fig. 2. Equivalent circuit of single DFIG infinite bus system.

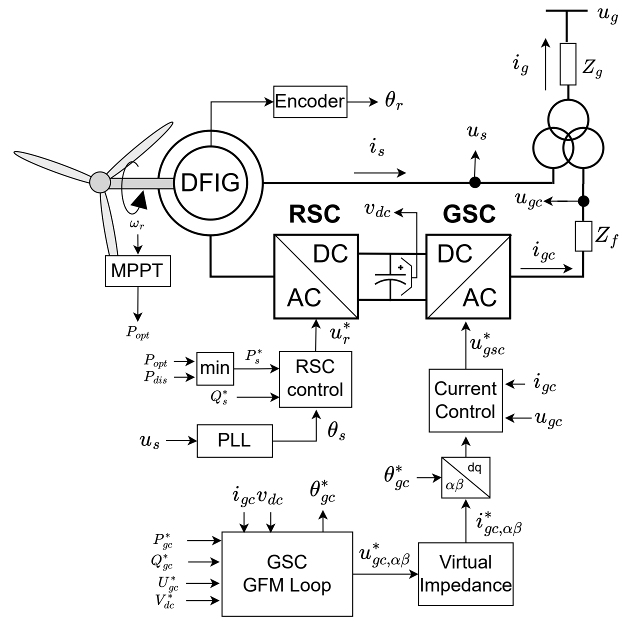

Fig. 3. Diagram of GFM DFIG based on GSC.

the capability of DC bus voltage control and almost-global synchronization stability [14] . The fVOC is originally implemented in the stationary reference frame. For the convenience of subsequent analysis, it is converted into polar coordinates:

$$\begin{aligned}
\frac{\mathrm{d}}{\mathrm{d}t}\theta_{gc}^* &= \omega_g + \eta\left(\sin\rho\Delta p - \cos\rho\Delta q\right), \\
\frac{\mathrm{d}}{\mathrm{d}t}\|\boldsymbol{u}_{gc}^*\| &= \|\boldsymbol{u}_{gc}^*\|\left[\eta\left(\cos\rho\Delta p + \sin\rho\Delta q\right)\right] \\
&\quad + \|\boldsymbol{u}_{gc}^*\|\alpha(1 - \|\boldsymbol{u}_{gc}^*\|^2/U_{gc}^{*2}),
\end{aligned} \tag{2}$$

where, $\Delta p = P_{gc}^*/U_{gc}^{*2} + \lambda(v_{dc} - V_{dc}^*) - p_{gc}/\|\boldsymbol{u}_{gc}^*\|^2$ and $\Delta q = Q_{gc}^*/U_{gc}^{*2} - q_{gc}/\|\boldsymbol{u}_{gc}^*\|^2$. The instantaneous active and reactive powers of fVOC are calculated as $p_{gc} = \|\boldsymbol{u}_{gc}^*\| i_{d_g,gc}$ and $q_{gc} = -\|\boldsymbol{u}_{gc}^*\| i_{q_g,gc}$,. Then, virtual impedance is employed to generate current commands.

$$\begin{bmatrix} i_{d_g,gc}^* \\ i_{q_g,gc}^* \end{bmatrix} = \begin{bmatrix} r_{vi} & -x_{vi} \\ x_{vi} & r_{vi} \end{bmatrix}^{-1} \begin{bmatrix} u_{d_g,gc}^* - u_{d_g,gc} \\ u_{q_g,gc}^* - u_{q_g,gc} \end{bmatrix} \tag{3}$$

P_{gc}^* is set to $P_{gc,0}^* = -sP_s^*$ to enhance the control performance of v_{dc}.

979-8-3315-8138-1

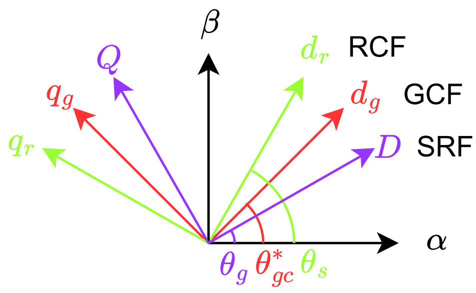

Fig. 4. Reference frames

III. Synchronization Stability Analysis

The control of the GSC and RSC is performed in their respective reference frames. As a result, there are one stationary reference frame $\alpha\beta$ and three rotating reference frames (Fig. 4). The synchronous reference frame (SRF) is represented by subscripts D, Q. The d-axis of RSC control reference frame (RCF), noted by subscripts d_r, q_r, is aligned along θ_s tracked by the PLL. The GSC is controlled in the grid-side reference frame (GCF) given by the GFM Loop, noted by subscripts d_g, q_g. The rotation matrix $\mathcal{R}(\theta)$ (4) is employed for the transformation of vectors between different reference frames. Specially, $\mathcal{R}(\pi/2)$ is labeled as $\mathcal{J}$.

$$\mathcal{R}(\theta) = \begin{bmatrix} \cos(\theta) & -\sin(\theta) \\ \sin(\theta) & \cos(\theta) \end{bmatrix} \tag{4}$$

The analysis in this section focuses on synchronization stability. The dynamics of the current control loop and the transmission lines are neglected. The Dynamics of the PLL is expressed as:

$$\theta_s = \frac{1}{\mathrm{s}} \left[\omega_g + (k_{p,PLL} + k_{i,PLL}\frac{1}{\mathrm{s}}) \right] u_{q_r,s} \tag{5}$$

The power controller is:

$$\begin{aligned} i_{d_r,s} &= (k_p + k_i \frac{1}{\mathrm{s}}))(P^*_s - p_s), \\ i_{q_r,s} &= -(k_p + k_i \frac{1}{\mathrm{s}}))(Q^*_s - q_s), \end{aligned} \tag{6}$$

The stator power is calculated as $p_s = \boldsymbol{u}_{s\top} \boldsymbol{i}_s, q_s == \boldsymbol{u}_{s\top} \mathcal{J} \boldsymbol{i}_s$. Neglecting losses, the rotor power is approximated as $p_r = -s p_s$. The dynamics of DC bus voltage is expressed as:

$$\frac{\mathrm{d}}{\mathrm{d}t} v_{dc} = \frac{1}{c_f v_{dc}} (p_r - p_{gc}). \tag{7}$$

As the dynamics of inner current loops are neglected, the dynamics of the GSC are described by (2). By Park transformation, vectors in control reference frames are transformed to SRF $\boldsymbol{u}^*_{gc,SRF} = \mathcal{R}(\theta^*_{gc} - \theta_g)\boldsymbol{u}^*_{gc,CRF}$, $\boldsymbol{i}_{s,SRF} = \mathcal{R}(\theta_s - \theta_g)\boldsymbol{u}^*_{gc,RRF}$. The inputs of the above differential equations in SRF, $\boldsymbol{u}_{s,SRF}$ and $\boldsymbol{i}_{gc,SRF}$, can be calculated based on the network current-voltage equations.

$$\begin{bmatrix} \boldsymbol{u}_{s,SRF} \\ \boldsymbol{i}_{gc,SRF} \end{bmatrix} = \begin{bmatrix} \mathbf{I} & -\boldsymbol{Z}_g \\ \mathbf{0} & -\boldsymbol{Z}_{gc} \end{bmatrix} \begin{bmatrix} (\mathcal{J} x_{Ts} + \boldsymbol{Z}_g)\boldsymbol{i}_{s,SRF} + \boldsymbol{u}_{g,SRF} \\ -\boldsymbol{u}^*_{gc,SRF} + \boldsymbol{Z}_g \boldsymbol{i}_{s,SRF} + \boldsymbol{u}_{g,SRF}, \end{bmatrix} \tag{8}$$

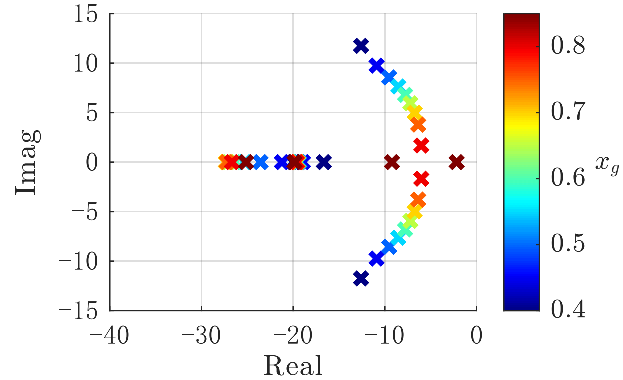

Fig. 5. The trajectory of dominant eigenvalues as x_g increases.

TABLE I
Participation Factor Analysis

Eigenvalues	states	Participation Factor
$-6.36 \pm 3.79j$	θ^*_{gc}	0.49
	v_{dc}	0.48
-19.54	x_{pll}	0.86
	θ_s	0.08
-27.24	$\lVert \boldsymbol{u}^*_{gc} \rVert$	0.64
	θ^*_{gc}	0.14

where $\mathbf{I}$ is a 2×2 identity matrix. $\boldsymbol{Z}_g = \mathbf{I} r_g + \mathcal{J} x_g$ and $\boldsymbol{Z}_{gc} = \mathbf{I}(r_{vi} + r_f) + \mathcal{J}(x_{vi} + x_f + x_{Tgc})$ are the impedances of the transmission line and the GSC branch, respectively. Then, they are transformed to the control reference frames $\boldsymbol{u}_{s,RCF} = \mathcal{R}(\theta_g - \theta_s)\boldsymbol{u}_{s,SRF}$, $\boldsymbol{i}_{gc,GCF} = \mathcal{R}(\theta_g - \theta^*_{gc})\boldsymbol{i}_{gc,SRF}$.

Based on above equations, the state-space model of the system is established $\dot{\boldsymbol{x}} = \boldsymbol{f}(\boldsymbol{x})$. The synchronous stability of the system is characterized by the distribution of eigenvalues of the system matrix $\mathbf{A} = \partial \boldsymbol{f}(\boldsymbol{x}) / \partial \boldsymbol{x}^\top$.

The trajectory of dominant eigenvalues of $\mathbf{A}$ with x_g varies is shown in Fig. 5.

Table I gives the participation factor with $x_g = 0.75$ p.u.. The eigenvalue associated with the PLL moves away from the imaginary axis as x_g increases. As grid strength decreases, the influence of the GFM GSC gradually increases. As a result, the PLL synchronization capability also does not weaken. Meanwhile, the eigenvalue associated with $\lVert \boldsymbol{u}^*_{gc} \rVert$ moves away from the imaginary axis. This is also because the voltage regulation capability of GFM GSC is stronger under weak grid conditions. The pair of complex eigenvalues are mainly related to fVOC phase angle θ^*_{gc} and DC bus voltage v_{dc}. As x_g increases, they gradually move towards the imaginary axis. The fVOC achieves phase angle synchronization based on power, while the DC bus voltage is closely related to the GSC power. Therefore, these two states are clearly coupled, and the eigenvalues associated with them are the closest to the imaginary axis. Considering this, the trajectories of the eigenvalues of $\mathbf{A}$ with changes in c_f under different grid strength are shown in Fig. 6. Increasing c_f can improve the stability of the DC bus voltage. However, a large c_f may cause other modes to move closer to the imaginary axis.

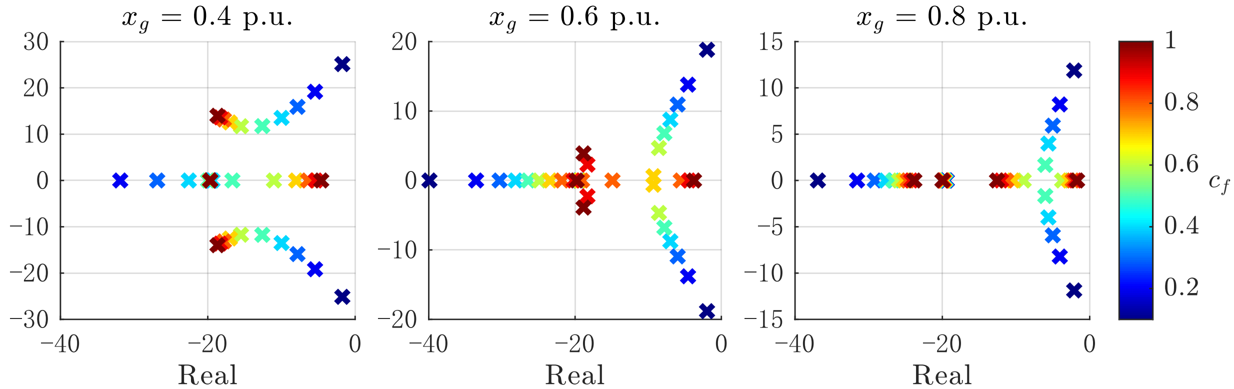

Fig. 6. The trajectory of dominant eigenvalues as c_f increases .

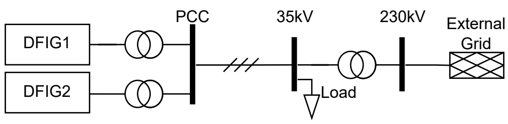

Fig. 7. Test system

IV. Simulation Test

We implemented the proposed GSC-based GFM control in PSCAD/EMTDC; the single-line test system is shown in Fig. 7. The base model follows [15] and key parameters are listed in Appendix A. The parameters could be further optimized for transient performance by optimization metrics [16], but this is not the focus of this paper.

Three cases are considered: (A) both units in GFL; (B) DFIG1 switches to GFM at 7.5 s after DFIG2 reaches 1.0 p.u.; (C) DFIG1 is already in GFM before DFIG2 starts. As shown in Fig. 8a, when DFIG2 reached its active power set-point, the stator voltage dropped to 0.85 p.u. At the same time, excessive transmitted active power weakens the synchronization capability of PLL, causing the system to begin oscillating and approach an unstable state. At this point, small disturbances could lead to PLL synchronization failure, resulting in system collapse. In contrast, the results of Case B and Case C demonstrate the effectiveness of the proposed RSC-based GFM control method As shown in Fig. 8b, after DFIG1 switched to grid-forming mode, the oscillations disappeared directly, even though there was no significant change in the stator voltage. In Fig. 8c, when DFIG1 switched to GSC GFM mode before DFIG2 started, the startup and active power generation increase of DFIG2 similarly reduce the stator voltage, but the system does not experience any oscillations. GSC GFM DFIG provides time for the system to employ secondary regulation to recover the voltage. The above results show that the proposed method can effectively enhance the stability of DFIG under weak grid conditions and improve the power delivery capability.

We simulated the dynamic response of the system under varying external wind speeds. The results is shown in Fig. 9. The initial wind speed was 11 m/s, with 1.0 p.u. active power generation. At 4.0 second, the wind speed suddenly dropped to 6 m/s, causing the rotor speed to decrease. Consequently, the power reference value provided by the mechanical system decreased. During this process, the output active power always followed the MPPT power command. Meanwhile, the DFIG gradually transitioned from super-synchronous to sub-synchronous. At 12.5 seconds, the wind speed suddenly increased to 9 m/s, and the DFIG gradually transitioned back to super-synchronous.

V. Conclusions

Based on the Thevenin equivalent, this paper proposes a GFM strategy for DFIGs using GSC. The method enhances system stability under weak grid conditions without compromising the power control performance of the stator side. Synchronous stability analysis demonstrates that as grid strength decreases, the influence of the GFM GSC on the stator voltage gradually increases, ensuring the synchronization capability of the phase-locked loop (PLL) in weak grids. Simulation experiments conducted in PSCAD/EMTDC validate the effectiveness of the proposed method. The approach enables the GSC to exhibit voltage source characteristics. Future research may focus on designing stator power control strategies to automatically match external loads and achieve islanded operation.

Acknowledgment

This work was supported by the Science and Technology Project of State Grid (4000-202429062A-1-1-ZN).

Appendix
Main Parameters

1) Base values: S_{base} =2 MWA, $U_{s,base} = 690V$.
2) Transmission line and induction machine parameters: $x_g = 0.4$,$r_g = 0.01$,$x_{Ts} = 0.01$,$x_{Tgc} = 0.01$,$x_f = 0.05$,$r_f = 0.001$
3) GSC parameters: $\eta = 15$, $\alpha = 10$, $\lambda = 2$,$\rho = 5\pi/6$,$x_{vi} = 0.25$,$r_{vi} = 0.1$

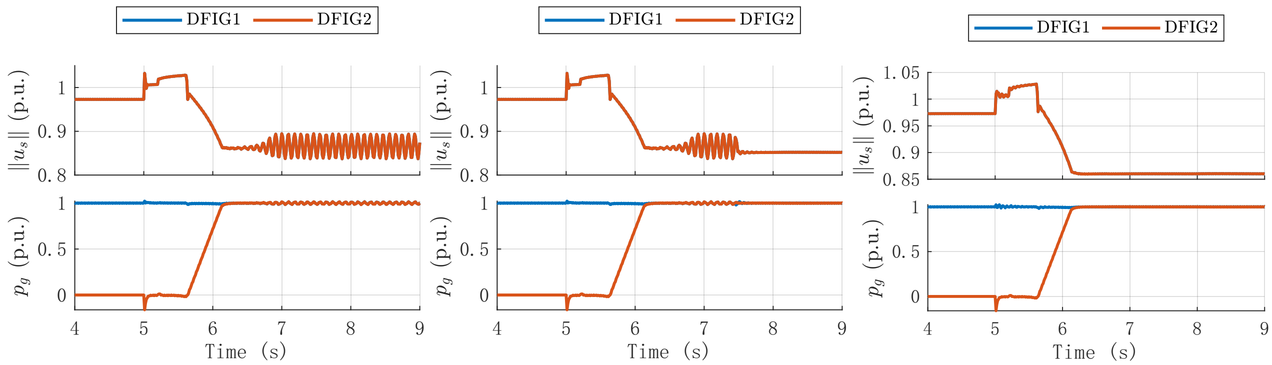

(a) Case A (b) Case B (c) Case C

Fig. 8. Start-up process simulation of DFIG2.

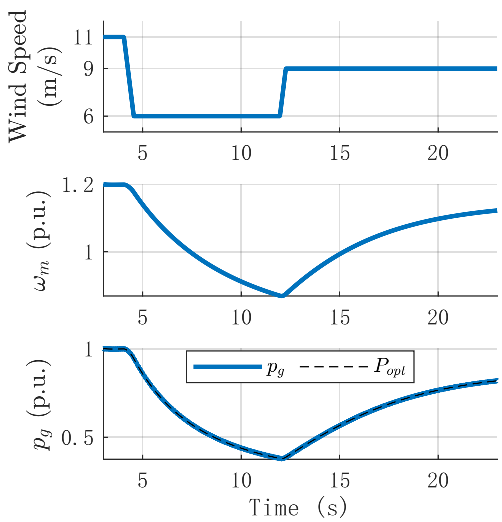

Fig. 9. Simulation results of GSC GFM DFIG under varying wind speeds.

REFERENCES

[1] X. Wang, M. G. Taul, H. Wu, Y. Liao, F. Blaabjerg, and L. Harnefors, "Grid-synchronization stability of converter-based resources—an overview," *IEEE Open Journal of Industry Applications*, vol. 1, pp. 115–134, 2020.

[2] X. Guo, D. Zhu, X. Zou, Y. Yang, Y. Kang, W. Tang, and L. Peng, "Analysis and enhancement of active power transfer capability for dfig-based wts in very weak grid," *IEEE Journal of Emerging and Selected Topics in Power Electronics*, vol. 10, no. 4, pp. 3895–3906, 2022.

[3] H. Nian and B. Pang, "Stability and power quality enhancement strategy for dfig system connected to harmonic grid with parallel compensation," *IEEE Transactions on Energy Conversion*, vol. 34, no. 2, pp. 1010–1022, 2019.

[4] M. CHEN, K. WANG, Y. SHEN, Z. ZENG, X. LIN, and Q. SONG, "Comparison of grid-forming control solutions for offshore wind farms connected with diode rectifier-based high voltage dc transmission," *Electric Power*, vol. 58, no. 5, pp. 166–175, 2025.

[5] S. Shah and V. Gevorgian, "Control, operation, and stability characteristics of grid-forming type iii wind turbines," in *19th Wind Integration Workshop*, 2020.

[6] W. Yan, S. Shah, V. Gevorgian, P. Koralewicz, R. Wallen, and D. W. Gao, "On the low risk of ssr in type iii wind turbines operating with grid-forming control," *IEEE Transactions on Sustainable Energy*, vol. 15, no. 1, pp. 443–453, 2024.

[7] S. Wang, J. Hu, and X. Yuan, "Dfig-based wind turbines with virtual synchronous control: Inertia support in weak grid," in *2015 IEEE Power & Energy Society General Meeting*, 2015, pp. 1–14.

[8] Z. Li, Z. Xie, and X. Zhang, "An improved strategy of grid-forming dfig based on disturbance rejection stator flux control," *IEEE Transactions on Industrial Electronics*, vol. 71, no. 3, pp. 2498–2509, 2024.

[9] L. Huang, H. Xin, L. Zhang, Z. Wang, K. Wu, and H. Wang, "Synchronization and frequency regulation of dfig-based wind turbine generators with synchronized control," *IEEE Transactions on Energy Conversion*, vol. 32, no. 3, pp. 1251–1262, 2017.

[10] Z. Li, Z. Xie, S. Xu, and X. Zhang, "Improving transient stability of grid-forming dfig based on enhanced hybrid synchronization control," *IEEE Transactions on Industrial Electronics*, vol. 71, no. 12, pp. 15 881–15 894, 2024.

[11] S. Wang and L. Shang, "Fault ride through strategy of virtual-synchronous-controlled dfig-based wind turbines under symmetrical grid faults," *IEEE Transactions on Energy Conversion*, vol. 35, no. 3, pp. 1360–1371, 2020.

[12] M. Li, Z. Xie, S. Xu, S. Yang, and X. Zhang, "Electromechanical oscillation analysis and suppression of grid forming dfig-based wind turbines under weak grid," *IEEE Transactions on Energy Conversion*, vol. 40, no. 2, pp. 1365–1377, 2025.

[13] G. Abad, J. Lopez, M. Rodriguez, L. Marroyo, and G. Iwanski, *Doubly fed induction machine: modeling and control for wind energy generation*. John Wiley & Sons, 2011.

[14] Z. Guo, W. Wu, and G. Wu, "Full-state virtual oscillator control for grid-forming pvs to endure solar radiation and grid disturbances," *IEEE Transactions on Energy Conversion*, vol. 40, no. 3, pp. 2576–2586, 2025.

[15] PSCAD Team. (2018) Type 3 wind turbine generators (wtg) (for pscad v4.6). Manitoba Hydro International Ltd. [Online]. Available: https://www.pscad.com/knowledge-base/article/496

[16] C. ZHANG, J. YU, M. SHI, and R. LIU, "Analysis and optimization of voltage dynamic control performance of renewable energy microgrid based on grid-forming energy storage," *Electric Power*, vol. 58, no. 9, pp. 115–123, 2025.

979-8-3315-8138-1